Peter Journey-Kilarney

Photoaction Current Spectra of Polymer Solar Cells

Thesis submitted in partial fulfillment of the requirements of the degree of Bachelor of Science in Physics

UC Santa Cruz

June 2001

Abstract:

For my thesis I have investigated the photoaction current spectra of six different polymer solar cell configurations, to determine how different polymer / electron-collector architectures affect a solar cell's external quantum efficiency (efficiency at converting absorbed photon energy into electrical energy). Photoaction current spectra are taken by monitoring a solar cell's current output while varying the color of the light impinging on the cell. This allows external quantum efficiency (EQE) to be calculated as a function of the wavelength of the light absorbed by the solar cell. For this report I examined two different semiconducting polymer configurations, M3EH – PPV and a blend of M3EH – PPV and Cn – Ether - PPV. Each of these polymer configurations was examined with three different electron-collector configurations, a titanium oxide film (TiO_x), titanium dioxide nanoparticles (TiO_2), and combination of TiO_2 nanoparticles spread over a TiO_x film. For the M3EH solar cells it was noted that EQE performance was much better for devices with a TiO_2 / M3EH interface. TiO_x devices gave a peak EQE of 6.56% at 480nm, while TiO_2 devices generated a peak EQE of 16.87% at 460nm. The TiO_x / TiO_2 / M3EH devices gave the highest EQE for this experiment, with a peak EQE of 19.94% at 470nm. This data supports the argument that that TiO_2 nanoparticles increase the contact area between the polymer and electron-collector. Blended solar cells on TiO_x outperformed M3EH cells on TiO_x with a peak EQE of 18.34% at 500nm for blended versus only 6.56% at 480nm for M3EH. However, unlike the M3EH cells, the blends actually performed worse when a TiO_2 interface was used. Peak EQE dropped from

18.34% at 500nm to 11.23% at 480nm for the TiO_2 interface and fell to 11.98% at 460nm for the TiO_x / TiO_2 interface. This data indicates that for TiO_x the blending of the polymers enhances solar cell EQE. However, when TiO_2 is used blend EQE actually drops below M3EH EQE. This indicates that the interaction between the Cn – Ether and TiO_2 damages solar cell performance.

Introduction:

As human population continues to grow and the use of energy consuming technologies becomes more and more prevalent around the world, there is an increasing need for the efficient and reliable production of electrical energy. Currently world energy production is dominated by the consumption of fossil fuels. Although there is an established infrastructure for the conversion of fossil fuels into electricity, this system has several major drawbacks. Centrally, fossil fuels are non-renewable resources. While estimates vary on how long our surpluses of coal, oil and natural gas will last; the simple truth is that eventually these supplies will run out. In addition to their limited quantities, fossil fuels generate large amounts of pollution that endanger our environment and the health and safety of the world's populace. Nuclear fission is the other major power source for world energy production. If properly run and maintained nuclear power plants provide a relatively clean and highly efficient source of electricity. However, nuclear fuel is also a non-renewable resource and incidents such as Chernobyl and Three Mile Island raise important questions about the safety and environmental risks of nuclear power. The storage of spent reactor fuel is expensive and introduces yet another risk of contaminating the environment. The environmental and safety risks of fossil and nuclear

fuels and the worries over their limited supplies can be alleviated by shifting the world's energy production to clean and renewable sources of energy.

Among the many forms of renewable energy available for conversion into electricity, solar, wind, geothermal and hydroelectric are the most likely candidates to safely and reliably fill our energy needs. All of these resources can be harnessed without generating harmful pollution, all are virtually unlimited in supply, and the technologies needed to convert these resources to electrical energy are all established and currently in use.

Solar power has a number of advantages over other renewable resources. While wind, geothermal and hydroelectric power systems are limited to specific geographic regions containing the appropriate power source, solar power can be collected at almost any location on the earth. The systems for converting wind, heat and water into electricity are all centrally dependant on complex moving parts such as turbines and generators, which operate at high speeds, are prone to failure and require regular maintenance. Solar power systems are mechanically passive; electricity is produced simply by absorbing sunlight, making the systems virtually maintenance free. Solar power systems can be automated to increase collection efficiency, but the machinery involved works at low speeds and is easier and less expensive to maintain. One of the greatest advantages of solar power is that it can be produced on sight, eliminating the need for centralized power plants and a high maintenance electrical infrastructure. Solar power's numerous benefits have led to a large increase in its use over the last several decades. Unfortunately, there are still shortcomings to current solar cell technology,

which limit the expansion of solar power. Most notably, an increase in the use of solar power is restrained by the high cost of current solar power systems.

Most current solar cell systems are based on semiconducting silicon. Darryl Chapin and Cal Fuller first developed silicon solar cells in the 1950's at Bell Laboratories. These cells achieved energy conversion efficiencies (photon energy to electrical energy) of 6% by the mid-Fifties and continuing research has brought the efficiencies of modern silicon cells up to 29%, with most commercial systems operating at around 15%.[i] These systems are efficient enough to deliver reliable electric power; the drawbacks are in the cost and weight. Due to high manufacturing costs, silicon power systems are very expensive, greatly limiting the number of people who can afford solar power. The weight and size of silicon solar panels further increases the expense, especially on large-scale projects. To address these weight and cost problems, research is being conducted into several alternative types of solar cells.

One area of particular interest is that of polymer solar cells, which are based on semiconducting polymers first discovered in the late 1970s. Polymer solar cells have the advantages of being thinner, lighter and less expensive to manufacture than silicon solar cells. These properties could allow polymer solar cells to rapidly accelerate the growth of solar power, even opening the possibility that solar power will replace dangerous and polluting energy sources. However, before polymer solar cells can enter into commercial use, more research is needed to improve their efficiency. It is my goal to assist in improving polymer solar cell efficiency by investigating the photoaction current spectra (PACS) of several different polymer solar cell architectures. PACS give a solar cell's external quantum efficiency (photon energy to electrical energy) as a function of the

wavelength of the light impinging on the cell. For my thesis I will be examining the PACS of solar cells manufactured using two different conjugated polymers, M3EH – PPV and Cn – Ether – PPV. The polymer structures are shown below in Figs. 1a and 1b.

Fig. 1a: M3EH-PPV B157

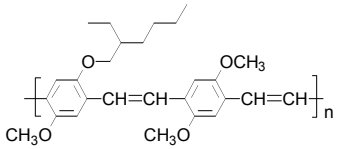

Poly[2-methoxy-5-(2-ethylhexyloxy)-1,4-phenylene-ethenylene-2,5-dimethoxy-1,4-phenylene-ethenylene]

Fig. 1b: CN-Ether-PPV HAT 94 N3/5

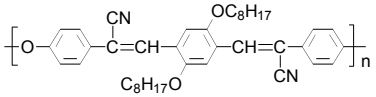

Poly[oxa-1,4-phenylene-1,2-(1-cyano)-ethenylene-2,5-dioctyloxy-1,4-phenylene-1,2-(2-cyano)-ethenylene-1,4-phenylene]

Polymers are the central component of a solar cell, the photoactive layer, where absorption of the incident light takes place. Conjugated polymers consist of chains of carbon atoms with alternating single to double bonds. This chain structure can be thought of as a periodic lattice, with one free electron per lattice site to facilitate conduction. However, the alternating bond structure breaks the symmetry of the lattice, creating an energy bandgap and leaving a filled conduction band and an empty valence band. At non-zero temperature the polymer behaves as a semiconductor. Like all semiconductors, polymers can be made conducting by doping them with mobile charge carriers. This can be achieved through several methods, chemical, electro-chemical, charge injection or photodoping. M3EH – PPV and Cn – Ether – PPV utilize the photodoping method. When light impinges on the polymer, electrons in the valence / highest occupied molecular orbital (HOMO) absorb photons with energy greater than or equal to the polymer's bandgap. These electrons jump into the conduction / lowest

unoccupied molecular orbital (LUMO), leaving holes in the HOMO. Thus the absorption of a photon generates an electron / hole pair, called an exciton, that can be exploited for charge transport. By sandwiching our polymer between two materials with the appropriate quantum work functions we can disassociate the exictons (separate the charge carriers) and conduct them out of the polymer. This process establishes an electric potential across the polymer layer. When the cell is connected to an external circuit this potential can be exploited to generate an electric current.

Solar Cell Structure: The various solar cells I will investigate all have a similar sandwich structure, with the layers composing a cell deposited one by one on top of a glass substrate. Fig. 2 below gives the structure common to all cell types.

Au Cathode / Hole Collector
Polymer
Electron Collector
Indium Tin Oxide (ITO) Anode
Glass Substrate

Fig. 2: Basic Sandwich Structure for all Cell Types

The glass substrate acts as backbone, supporting the cell. The indium tin oxide (ITO) layer is a transparent metal and acts as the cell's anode. The next layer of the cell is used to collect electrons from the polymer layer. The polymer layer is the central layer of the cell, absorbing light for conversion into electricity. The final Au layer acts as both the hole-collector and the cell's cathode. For my thesis I will examine how variations in

the polymer and electron-collector layers affect a cell's external quantum efficiency. I will consider two different polymer layer configuration, straight M3EH and a blend of 50% M3EH / 50% Cn – Ether. Both of these polymer configurations will be investigated with three different types of electron-collection layers, a titanium oxide film (TiO_x), titanium dioxide nanoparticles (TiO_2), and a combination of TiO_2 nanoparticles spread over a TiO_x film. In total I will be testing six different device configurations, M3EH TiO_x, M3EH TiO_2, M3EH TiO_x / TiO_2, Blend TiO_x, Blend TiO_2 and Blend TiO_x / TiO_2.

Solar Cell Function: To begin I will outline the function of an M3EH TiO_x solar cell; this cell type clearly demonstrates the basic function of the six cell types I will explore. I will then detail the differences between the two polymers and finally, I will compare the three electron-collector configurations. The work functions for an ITO / TiO_x / M3EH-PPV / Au interface are given below in Fig. 3.

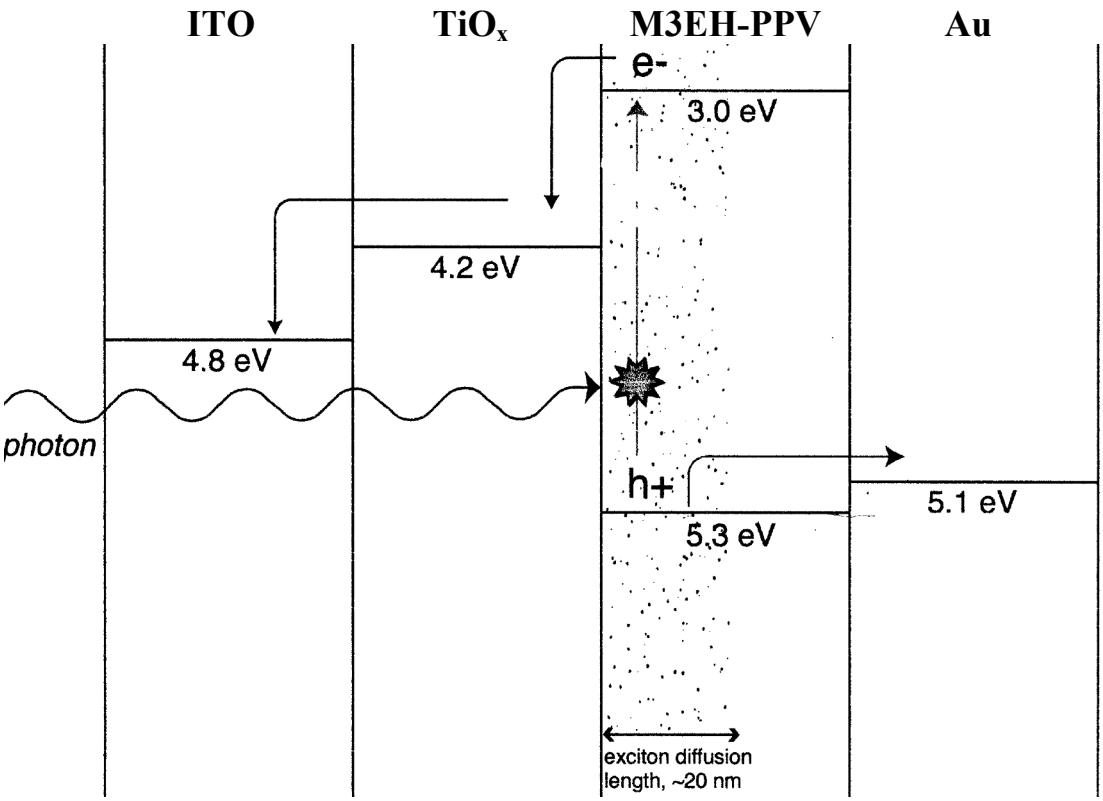

Fig. 3: Work Functions for a M3EH TiO_x Solar Cell[ii]

Photons are incident on the cell from the left; they travel through the ITO and TiO_x layers and are absorbed by the M3EH, generating excitons. For M3EH the exciton diffusion length is 20 nm. Electron / hole pairs generated within 20 nm of the TiO_x / M3EH disassociation interface can be separated. When excitons successfully separate, the holes are conducted to into the Au cathode while the electrons are conducted into the TiO_x layer and then step down again into the ITO anode. This generates a potential across the cell. If we connect an external circuit to the ITO and Au contacts we can draw current from the cell.

The TiO_x / M3EH / Au arrangement has several advantages. It provides good work functions for efficient exicton disassociation. The TiO_x layer also absorbs UV light that would otherwise damage the polymer. M3EH's light absorption drops off exponentially with thickness, thus most of the exictons are generated close to the TiO_x / M3EH disassociation interface. M3EH has much higher hole mobility than electron mobility, thus our configuration, with light impinging on the TiO_x / polymer interface is advantageous because the slower moving electrons have less distance to cover than the fast moving holes.

Blended M3EH / Cn - Ether: The blended polymer solar cells use the same architecture as the straight M3EH devices, except that the polymer layer is a one to one blend of M3EH and Cn- Ether. Blends function in the same manner as straight M3EH cells. Holes are conducted into the Au cathode while electrons move from the TiO_x layer to the ITO anode. When the polymers are blended they phase separate, forming distinct regions

of each polymer type. This separation generates a large contact area between the polymers, increasing the cell's exciton-disassociation boundaries. Thus, the excitons have a greater chance of separating, which can boost the performance of the cell. Because the two polymer types are blended it is not possible to draw a single work function extending from the TiO_x to the Au.

Electron-collector Configurations: For my thesis I will examine three different types of electron-collecting layers. All three are based on titanium oxide, a semitransparent semiconductor, which absorbs UV light. The first configuration is a layer of TiO_x. The x signifies that the exact nature of the oxygen bonding in the layer is unknown. The oxygen bonds form as the material is being applied to a substrate and generate a very smooth film (rms roughness 132Å)[iii]. The second possible configuration is a layer of TiO_2 nanoparticles, applied using a solution manufactured by Solaronix. In this solution the titanium dioxide particles are already formed, resulting in an applied layer that is very rough (rms roughness 268 Å)[iv] in comparison to a TiO_x layer. The roughness greatly increases the contact area between the electron-collector and the polymer layer, increasing a cell's exciton disassociations boundaries, which can boost the performance. The third configuration I will investigate is combination of TiO_2 layered over TiO_x.

Current Density versus Voltage Behavior: A great deal of information on a solar cell's performance can be learned from a cell's current density vs. voltage behavior (JV behavior), which can be obtained by taking JV curves of the cell. Fig. 4 on the following page gives a generic JV curve.

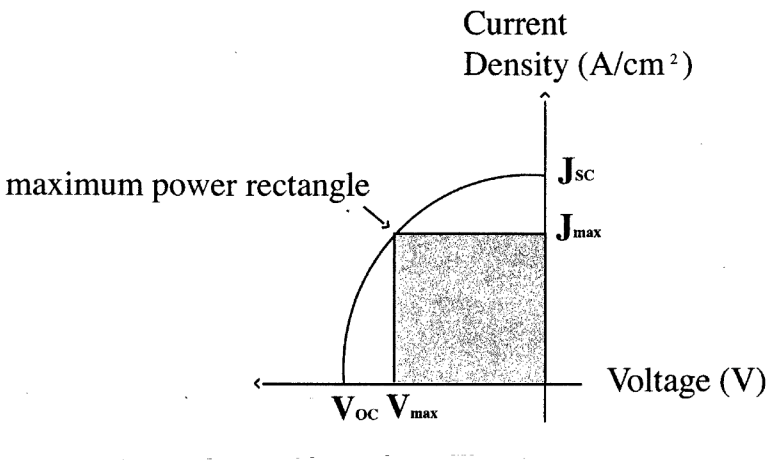

Fig. 4: Current Density versus Voltage Curve

J_{sc}, the short circuit current density, is the current density measured with no applied voltage (V = 0) and is a direct measure of the number of excitons generated by the cell. V_{oc}, the open circuit voltage, is measure of the voltage potential across the cell when no current is flowing (I = 0). Both of these values are directly proportional to the incident light intensity, with V_{oc} limited to the difference between the work functions of the anode and cathode and J_{sc} limited by the cell's EQE. The fill factor gives the peak performance of the cell normalized by (J_{sc} x V_{oc}) and is equal to,

$$ff = [(V \times J)_{max} / (V_{oc} \times J_{sc})] \times 100\% \quad (1)$$

For white light, the energy conversion efficiency over the entire solar spectrum is

$$\eta_p = (J_{sc} \times V_{oc} \times ff) / I \quad (2)$$

Where I is the optical power of the incident light. This efficiency is directly dependant on the external quantum efficiency (EQE) of the cell in question. EQE is a measure of the number of charge carrying pairs generated per number of incident photons absorbed. The maximum EQE sets the upper limit for the short circuit current density of a cell. EQE is determined by taking photoaction current spectra (PACS), which measure the current density of a cell with respect to the wavelength of the impinging light.

For my thesis I will compare and contrast the PACS of M3EH TiO_x, M3EH TiO_2, M3EH TiO_x / TiO_2, Blend TiO_x, Blend TiO_2 and Blend TiO_x / TiO_2 solar cells. My goal is to increase our understanding of how the different polymers and electron-collector configurations affect EQE. Better understanding of how these factors affect external quantum efficiencies will help to improve the performance of polymer-based solar cells.

Experimental:

In this section, I will outline how the six types of solar cells (devices) are manufactured, and then discuss the process for acquiring current density versus voltage data. Finally, I will give a detailed description of the apparatus and procedure used to take photoaction current spectra of polymer based solar cells.

Manufacturing Devices:

In the following section I will describe the procedures used to manufacture M3EH and blended polymer devices. The basic manufacturing process for all six types of cells is the same and any differences are clearly noted.

Preparation Work:

Recycling old substrates: To save money, used substrates are often recycled. They are cleaned with ethanol and a razor blade, and then washed in warm water and soap.

Mixing sol gel: The TiO_x layer is applied using a sol gel solution, which is made in house. Sol gel solution is prepped by combining 10ml ethanol, 750ml titanium ethoxide, 250ml high purity H_2O, and 2-4 drops of HCL (enough to get a pH of 1-2). These ingredients are placed in a glass jar and mixed on a stir plate with no heat for at least 24 hours before application. Once the solution has been made, the sol gel must be constantly spun to prevent premature reaction between the HCL and titanium ethoxide.

Mixing Polymer: The various polymers used to make solar cells must be suspended in an organic solvent before they can be applied to a substrate. A 1.0% solution of M3EH-PPV is prepared by combining .01g of M3EH-PPV polymer with 1.0g of ChloroBenzene. These ingredients are stirred on a hot plate set to 40°C for at least 24 hours before application. (This process makes enough polymer solution for approximately eight devices.) Blended M3EH / Cn- Ether solutions are also mixed in ChloroBenzene using the above method, with a 1% solution using .005g of each polymer.

Building the Devices:

The glass substrates used as the backbone of the solar cell come with the indium tin oxide (ITO) layer already attached. See Fig. 5 on the following page.

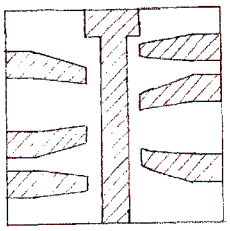

Fig. 5: Glass Substrate with ITO (shaded regions)

Masking the Substrates: The electron-collecting layer must be confined to the center strip of ITO. To confine the application the center ITO strip is masked off with tape.

Electron-Collection Layer: There are three possible configurations for the electron-collection layer, a titanium oxide film (TiO_x), titanium dioxide nanoparticles (TiO_2) and a combination of TiO_2 nanoparticles applied over a TiO_x film (TiO_x / TiO_2).

Spin Casting and Sintering sol gel / nanoparticles: A masked substrate is placed ITO face up on the spin caster and a pipetter is used to place the appropriate solution onto the substrate, TiO_x is applied using the sol gel solution, while TiO_2 is applied using the solution from Solaronix. The amount of solution used can be varied, but is normally around 100µl. The solution is spun at 1000 - 2000rpm for 40 seconds. The higher the spin speed used the thinner the layer of collector. Once the substrate has been spun, the tape mask is removed and the back of the substrate is cleaned with toluene. Next it is placed in a sintering oven at 230°C for 45 minutes.

Spinning the sol gel removes the ethanol, allowing the titanium ethoxide to react with the HCL, which forms TiO_x nanoparticles and some additional organic material. The sintering process removes these organics and helps the TiO_x particles to bond to each

other. The Solaronix solution does not react when spun, but sintering does remove the solvent and helps the nanoparticles to bond to each other.

Spin Casting and Annealing polymer: A sintered substrate is placed ITO face up on the spin caster and a pipetter is used to apply 40-80μl of the appropriate polymer (1% M3EH or .5% M3EH /.5% Cn – Ether). The polymer is spun at 1000 - 4000rpm. The higher the spin speed used the thinner the resulting polymer film will be. After spinning, the back of the substrate is cleaned with toluene, an organic solvent. Toluene is also used to expose the ITO contacts on the front of the cells. Next the substrates are placed in a vacuum oven, which is pumped down and heated to 100°C. The substrates are annealed in the oven for one hour. This process removes the ChloroBenzene solvent, leaving a layer of polymer distributed over the electron-collecting layer. Once the substrates have been annealed, they are placed in a nitrogen-filled glove box. This is done to prevent exposure to oxygen, which can form electron traps in the polymer, damaging device performance.

Gold Evaporation: The Au layer is applied to the substrate using an evaporation method. A set of four substrates is placed polymer-face down into a mask, which exposes six small strips for application of the gold. This mask is then placed in the evaporation chamber located inside the glove box. A small amount of gold is place in the evaporation boat located at the bottom of the chamber. The evaporation chamber is then sealed and pumped down to approximately $5x10^{-5}$tor. A high current is run through the boat to evaporate the gold. The evaporating gold adheres to the exposed surface of each substrate. The rate of gold deposition and the total deposition on the substrate are tabulated using a quartz crystal monitor. The current output is tuned to get a deposition

rate of approximately 0.5 – 1.0Å/sec and 400 - 600Å total deposition. The gold evaporation process completes the device. Each of the of the six gold strips creates an separate active area which can be independently tested. A completed device is illustrated below in Fig. 6.

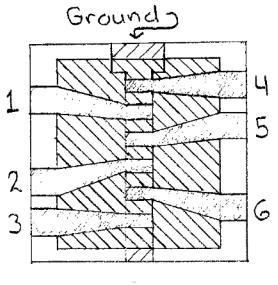

Fig. 6: Completed Device with 6 evaporated contacts, shaded region show polymer

Current Density vs. Voltage Curves:

Current density vs. voltage data (JV data) is taken using the JV apparatus and the JV section of the solar cell test station illustrated below in Figs. 7a and 7b.

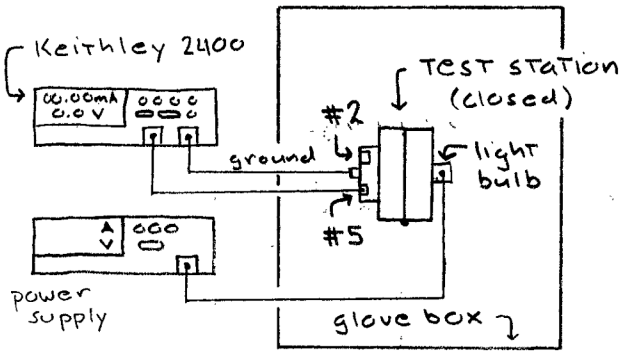

Fig. 7a: Current Density versus Voltage Apparatus

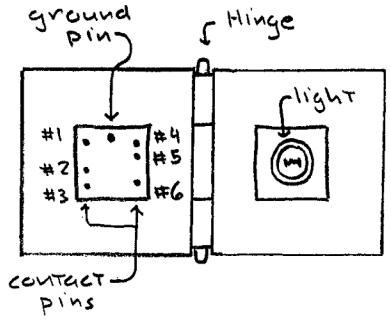

Fig. 7b: JV Test Station Detail

When a device is placed face down in the test station, the top "ground" pin touches the ITO contact and the other six pins touch the six evaporated Au contacts. Thus, the test station allows each of the six active areas to be independently connected to the Keithley 2400. The test station is hinged and can be closed to seal out all external light. The "door" of the test station holds a 4.8volt Xenon lamp, which acts as the light source for the JV data curves. The bulb has an output of approximately 70mW/cm^2. When the door is closed the bulb is located closest to the #2 and #5 active areas. Because these areas are closest to the bulb they generate the largest currents and are used to perform all JV testing.

To take JV curves the ground pin and the pin for the desired active area are connected to the Keithley 2400 SourceMeter, which is controlled by a LabView Virtual Instrument (VI) called 2400 Meas for Alexi. The Keithley applies a range of voltages across one of the active area and records the current generated at each voltage. The 2400 Meas for Alexi VI sets the initial, midpoint and final voltage, the magnitude of the voltage steps and the time between steps. All of these values can be varied, but for a typical JV data set initial voltage is set to –1.0V, midpoint to 1.0V and final to –1.0V with the Keithley taking .02V steps at a 150msec interval. This set up is used to perform two different types of JV curves, dark current and light current.

Dark Current: First, the device response is tested in the dark. Since there is no light exposure, no excitons are generated and the resulting current comes entirely from electrons that are forced through the polymer by the applied voltage. The dark current measurement gives us a "background" that can be subtracted from the light current to give the true photocurrent generated by the device.

Light Current: For these measurements the test station's light bulb is turned on. The polymer absorbs the light, generating a photocurrent. The Keithley monitors the current as the potential across the cell is varied. The current density versus voltage behavior of each active area is used to calculate the fill factor and power conversion efficiency of the device; this process is outlined in the introduction.

Photoaction Current Spectra Apparatus:

See Fig. 8 below for an illustration of the apparatus.

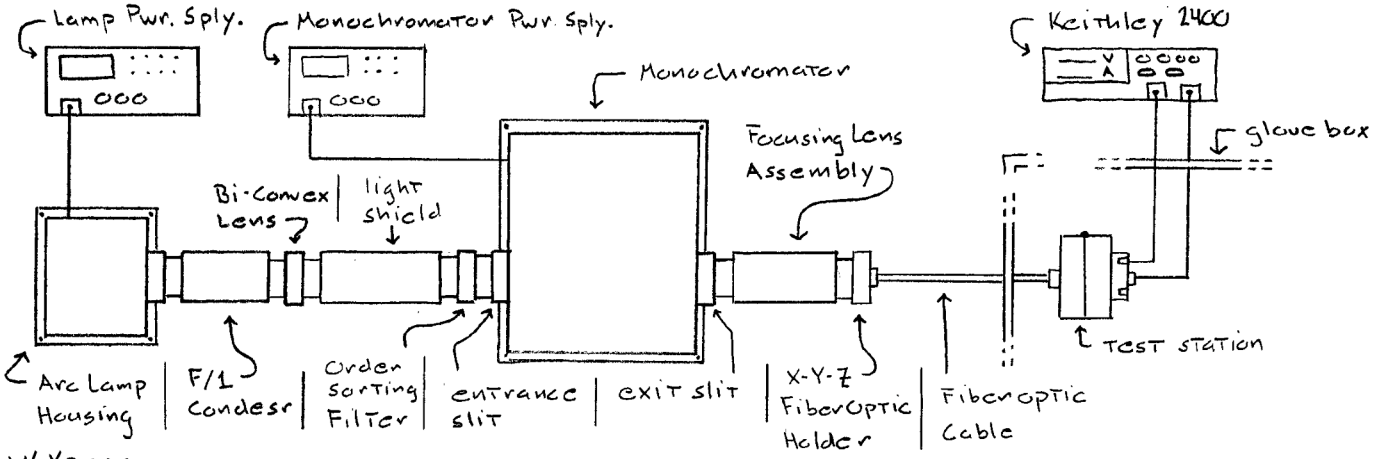

Fig. 8: Photoaction Current Spectra Apparatus

Oriel Arc Lamp Housing Model # 66902: The Lamp Housing contains the light source, a 150W Xenon arc lamp (Model # 6255) and an F/1 condenser, which collects the light from the lamp and collimates it into a coherent beam. The Lamp Housing is powered using an Oriel Arc Lamp Power Supply M#68907.

Oriel Bi-Convex Lens M# 41570: This is an F/4 fused silica lens with a 150mm focal length. It focuses the collimated beam from the Lamp Housing onto the monochromator's entrance slit. The Lens is mounted using an M# 6195 Oriel lens holder

Oriel Light Shield M# 71311: This is a tubular light shield, which extends from the Lamp housing output to the monochromator input. It contains the light path and blocks the entrance of any stray light.

Oriel Order Sorting Filter M# 51270: This is a high pass optical filter. It is used to eliminate ultraviolet light, which is damaging to the polymers layer of the solar cells. The filter is mounted using an M# 7123 Oriel filter holder.

Oriel Fixed Slits M# 77213: These slits are two identical slits, which mount directly to the monochromator. They act as input and output ports for the light and set the monochromator's resolution. The M#77213 pair has a 10nm resolution. These slits can be swapped with other Oriel slits to adjust the monochromator's resolution.

Oriel Corner Stone 130 1/8m Motorized Monochromator M# 74000: This is the central component of the apparatus. It is mounted on an Oriel M# 74006 mounting plate. A collimating mirror reflects light from the input slit is onto a diffraction grating. The diffracted light from the grating is then reflected onto the output slit by a focusing mirror. The size of the output slit determines the range of wavelengths (the resolution) of the light exiting the monochromator. The M# 74000 holds two gratings, which are mounted on a motorized turntable. The turntable is computer controlled and can be rotated to scan through output wavelengths. The monochromator is controlled using LabView.

Oriel Ruled Diffraction Gratings: The monochromator uses an M# 74024 ruled grating with a wavelength range from 200 – 1600nm and a peak efficiency of 85% and 350nm

(blaze wavelength) and an M# 74025 ruled grating with a 450 – 1600nm range and an 85% peak efficiency at 750nm. For my thesis I will be suing the M#74024 grating.

Grating Physics: Each grating consists of a substrate etched with a large number of parallel grooves coated in a reflective material. The quality and spacing of the grooves are crucial to the performance of the grating; however, the basic grating equation can be derived by considering a small cross section of the grating illustrated below in Fig. 9.

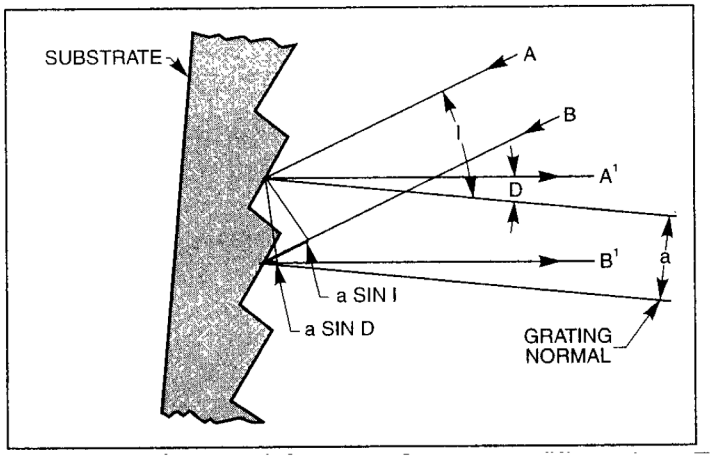

Fig. 9: Cross Section of Diffraction Grating with Incident and Reflected Rays

Light rays A and B, of wavelength λ are incident on adjacent grooves at angle I to the grating normal. The incident light is scattered at all angles, if we consider the light scattered at angle D we can see that the path difference between the diffracted rays A^1 and B^1 is given by

$$a (\sin I + \sin D) \qquad (3)$$

Where I and D are the angles described above and a is the spacing between grooves. A^1 and B^1 will interfere constructively if the path difference is equal to an integer multiple of the wavelength λ. The resultant grating equation can be written as follows.

$$a (\sin I + \sin D) = m\lambda \quad (4)$$

Where m is an integer giving the order of diffraction. When polychromatic light is incident on the grating it is dispersed such that each wavelength satisfies the grating equation. The input slit and collimating mirror of the M#74000 monochromator fix the light's input direction, while the focusing mirror and exit slit fix the output direction. The exit slit allows a small range of wavelengths to exit, the remainder of the light is scattered and absorbed inside the monochromator. As the grating is rotated the angles I and D change, but the difference between them is fixed by the monochromator's geometry. Thus a more convenient form of the grating equation is

$$m\lambda = 2a(\cos \phi \times \sin \theta) \quad (5)$$

Where ϕ is the half angle between the incident and diffracted ray and is set by the monochromator's geometry (ϕ= 5.1° for M#74000). θ is the grating angle relative to the zero order position and is controlled by rotating the grating. This gives an equation relating the angular position of the grating to the wavelength of the light output.

Oriel Rods M# 12312 and Rod holders M# 14421: The rods and rod holders form three height adjustable legs, which are used to connect the monochromator mounting plate to the optical breadboard and allow the vertical positioning of the monochromator.

Oriel Focusing Lens Assembly M# 77330: The focusing assembly is mounted directly to the monochromator's exit port. It holds a fused silica bi-convex lens (M# 39313), which takes the diverging output beam from the monochromator's exit slit and focuses it onto the fiber optic cable's input.

Fiber Optic Cable M#77566: This is a liquid filled cable, which transfers the monochromator's output into the nitrogen glove box and onto a device mounted in the solar cell test station. The cable is mounted with an Oriel M# 77802 X-Y-Z Fiber Optic Holder, which allows adjustment of the input position.

Solar Cell Test Station: The Photoaction current spectra (PACS) section of the test station is similar to the JV section and is illustrated below in Fig. 10.

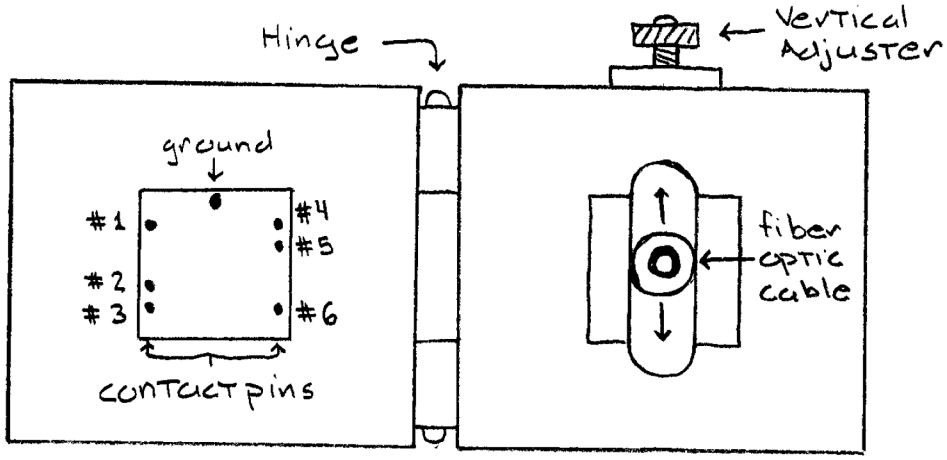

Fig. 10: Photoaction Current Spectra Test Station Detail

The PACS section of the test station uses the same seven-pin configuration as the JV section to establish contact with the six active areas of a device. In addition the PACS section has silicon photodetector mounted to the rear wall of the test station. This detector is used for calibration measurements. The "door" of the PACS section holds a mount for the fiber optic cable. This mount can be vertically adjusted to center the fiber output onto the Si detector or one of the device active areas.

Keithley 2400 Sourcemeter: The Keithley is connected to the test station contacts and measures the current output of each active area as the monochromator scans through the desired range of wavelengths.

Optical Bread Board: The arc lamp housing, monochromator and all associated optics are mounted on a metric optical breadboard. The breadboard facilitates proper placement of the components and allows them to be locked down.

Photoaction Current Spectra Procedure:

In this section I will discuss calibrating the photoaction current spectra apparatus (PACS apparatus) to maximize the transfer of light from the arc lamp to the test station. I will also outline the function of the LabView Virtual Instrument (VI) used to collect current density versus wavelength data (Jλ data). Finally, I will discuss how to take Jλ data for the Si detector and the device active areas and explain how this data is used to calculate the external quantum efficiency for a solar cell.

Calibrating The Photoaction Current Spectra Apparatus:

Before data can be collected it is necessary to properly calibrate the PACS apparatus so that its optical throughput is maximized. Note that UV protection must be worn while calibrating the apparatus.

Initial Setup: First the focusing lens and light shield are attached to the condenser of the arc lamp housing. Next the monochromator is mounted to the optical breadboard using the three height adjustable legs. The focusing lens assembly and fiber optic holder are connected to the monochromator exit port and the fiber optic cable is placed into the X-Y-Z holder. The 10nm slits are slipped into the entrance and exit slit holders on the monochromator. The arc lamp is switched on and the Si photodetector is hooked up to the Keithley 2400. The fiber optical cable is locked into the PACS section of the test station. The fiber output is centered on the Si photodetector by monitoring the current output of the detector with the Keithley 2400 and adjusting the fiber position until the detector current is maximized.

The various adjustments listed below are performed one by one while watching the current output of the Si detector. When the maximum current for a particular adjustment is reached that part of the apparatus is locked down and the next adjustment is begun.

Monochromator Height: The monochromator entrance slit must be vertically aligned with the output beam from the lamp housing. Three small jacks are placed between the monochromator mounting plate and the breadboard. The jacks are used to adjust the height of the monochromator until the collar of the light shield fits evenly over the slit holder on the monochromator and the current is maximal. A bubble level should be

placed on top of the monochromator to insure that it stays level. When the monochromator is at the optimal height the adjustable legs are locked down.

Monochromator to Lamp Housing Distance: The focusing lens on the lamp housing condenser has a 150mm focal length. A ruler is used to mark off 150mm perpendicular from the monochromator entrance slit and the arc lamp housing is placed such that the focusing lens is over the 150mm mark. The arc lamp's beam output is visually centered on the monochromator entrance slit (UV protection!). The current measurements from the detector are used to fine-tune the lamp housing's position. Once the maximum current is reached the lamp housing is locked into the breadboard.

Filter and Light Shield: Now that the monochromator and lamp are locked down, the order-sorting filter is attached to the monochromator entrance slit holder. Next the light shield is extended and connected to the filter holder.

Lamp Beam Collimation: The horizontal position of the condenser is adjusted using the black lever extending from the condenser. Once current is maximized the beam is collimated and the condenser is locked into place.

Focusing Lens Assembly: The lens assembly has a small metal lever, which adjusts the distance between the lens and the monochromator exit slit. The lever position is adjusted until you get the highest current. Unfortunately this lever cannot be locked down, so extra care is should be taken not to disturb its position.

Fiber Optic Cable: The fiber optic cable can be adjusted horizontally in and out of it housing and also vertically using the knobs on the housing. These adjustments are used to maximize the current and then the fiber is locked into place.

LabView Virtual Instrument:

The collection of Jλ data is automated using a LabView Virtual Instrument (VI), called photoaction 1.1. This VI has controls that allow the experimenter to select the desired grating, set the start and stop wavelengths of the range to be scanned over, set the wavelength increment for the scan, set the voltage to be applied to the active area and select the name/location of the output file. The VI uses simple GPIB read/write commands to communicate with and control the Keithley 2400 sourcemeter and the Oriel monochromator. The operation of the VI, listed below, details all the steps in acquiring Jλ data.

1: The VI sets the monochromator to the desired diffraction grating.

2: The VI activates the Keithley sourcemeter and sets it to the desired voltage.

3: The VI sets the monochromator's output to the start wavelength.

4: The VI pauses for 150ms to allow the device or detector to respond to the wavelength.

5: The VI reads the current generated at this wavelength from the Keithley and records a data set of wavelength x = current y.

6: The VI increases the monochromator's output by the set wavelength increment.

7: Steps 4, 5 and 6 are repeated until the monochromator's output is equal to the stop wavelength. The data set from each iteration is appended to the previous data set, generating a two-column list of wavelength versus current data.

8: The VI writes a spreadsheet file, containing the complete list of current versus wavelength data sets, to the name and location specified in the file name field.

9: The VI resets the monochromator's output to the start wavelength and reset the Keithley 2400 to zero bias.

Jλ Measurement Procedure and Calculation of External Quantum Efficiency:

In this section I will describe how Jλ data is collected for solar cells and for the Si detector. Then I will outline how the data is used to calculate EQE. Jλ data is collected and EQE tabulated for each of the six types of polymer solar cells. Before taking photoaction current spectra of a device, the device's JV behavior is tested to insure that the device is not shorted. In addition, it is preferable to choose devices, which exhibit good JV performance (high J_{SC} and high V_{OC}). These devices will generate Jλ data that is easier to observe and interpret.

Jλ Data Sets: The device of interest is placed face down inside the PACS section of the test station. First a Si calibration measurement is taken. The Si detector is connected to the Keithley 2400 and the fiber optic is inserted into the test station until it is flush against the face of the device, the fiber is then locked down. Next the fiber is vertically adjusted using the screw on the test station. When the current output of the Keithley is maximal the fiber is centered on the detector and calibration data can be taken. It is best to set the monochromator's output wavelength to 650nm when centering the fiber optic. This wavelength yields the highest current output from the detector, which greatly facilitates centering the fiber optic. Once the fiber optic is centered the photoaction 1.1 VI is run and generates a Jλ data file. For my thesis I will be scanning from 350nm – 700nm with a 10nm resolution.

Next the Keithley 2400 is connected to one of the device active areas. The fiber optic mount allows the fiber output to be centered over any of a device's six active areas. For my thesis I will try to concentrate on areas #2 and #5, as it is possible get JV data for

these areas, however, if #2 or #5 perform poorly other active areas will be tested. To get Jλ data for an active area the fiber output is centered on the area using the same method as above, with the Keithley connected to the area of interest and the monochromator output wavelength set to 470nm. When the fiber is centered the photoaction 1.1 VI is run and generates a Jλ data file for the active area. The scan for the device active area is identical to the Si calibration scan, 350nm – 700nm at 10nm resolution.

Jλ measurements are taken at a variety of applied voltages; zero bias data is always taken along with several positive and negative bias measurements. The magnitude of the +/- measurements is dependant on the type of solar cell being tested. These measurements can be used to gain additional information on the solar cell's performance. Unfortunately I do not have time to address the analysis of the biased measurements.

Calculating External Quantum Efficiency: The EQE of a device active area is calculated using the area's zero bias Jλ data and the Si Jλ data for that device. First the currents from theses two measurements are converted into current densities, dividing each current measurement by the respective area of photon collection. For a device, the active / collection area is $3mm^2$, for the Si detector the collection area is $4.9mm^2$. The following equation is then used to calculate the EQE of the device for each wavelength.

$$EQE_{DEVICE}(\lambda) = \{ J_{DEVICE}(\lambda) / J_{Si}(\lambda) \} \times EQE_{Si}(\lambda) \qquad (6)$$

Where J_{DEVICE} and J_{Si} are the current densities for the device area and Si detector and EQE_{Si} is the external quantum efficiency of the Si detector. The EQE of the Si detector

used for this calculation was determined by curve fitting data from The Nation Renewable Energy Lab (NREL) in Golden, Co. Fig. 11 below shows a graph comparing the curve fit to original NREL data. All the EQE calculations are performed using Kaleidagraph, which takes a set of device / Si Jλ data files and generates a file listing the wavelengths scanned and the corresponding EQEs.

Fig.11: NREL Silicon Data with Fit

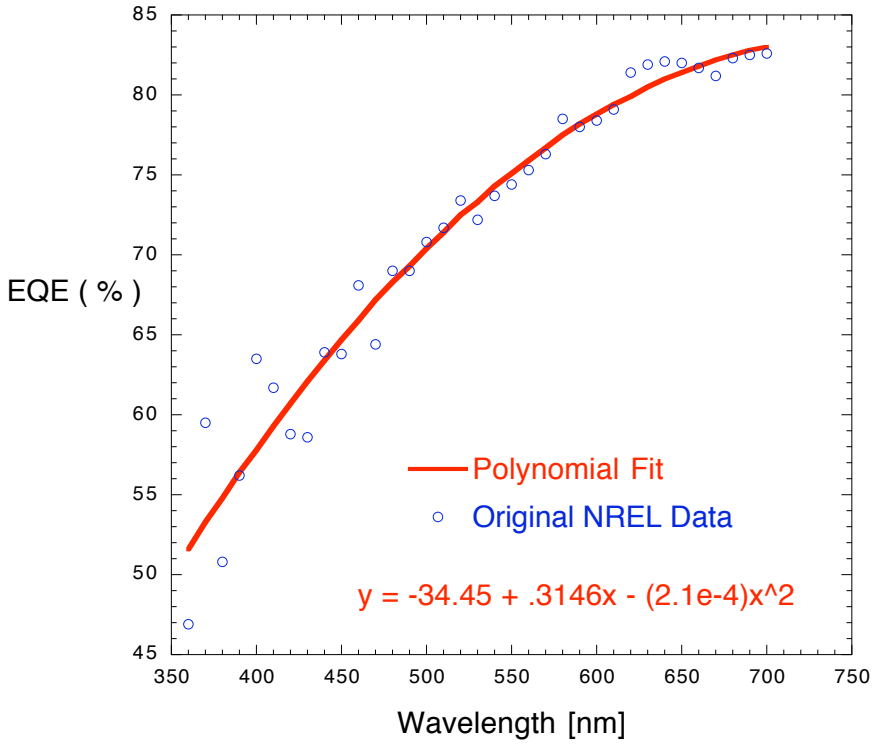

Data and Analysis:

In this section I will compare and contrast the external quantum efficiencies for the six solar cells configurations and offer some possible explanations for the variations in device performances. The devices I tested were manufactured by Stephanie V. Chasteen and Dr. Melissa Kreger. Tested devices will be labeled SVC (Stephanie) or

MK (Dr. Kreger) and will include a number. For example, SVC 402.5 indicates that this is Stephanie's device #402 and that area #5 is being investigated.

First I will outline the EQE performances of the M3EH devices. Showing the range of EQEs for each of the three electron-collector configurations and making an overall comparison between the best of the M3EH TiO_x, M3EH TiO_2 and M3EH TiO_x / TiO_2 devices. Next I will outline the EQE performances of the blended devices. Once again, showing the range of EQEs and giving an overall comparison of the Blend TiO_x, Blend TiO_2 and Blend TiO_x / TiO_2 devices. Finally, I will compare M3EH and blended devices with similar electron-collectors.

Fig.12: M3EH TiOx EQE Comparison

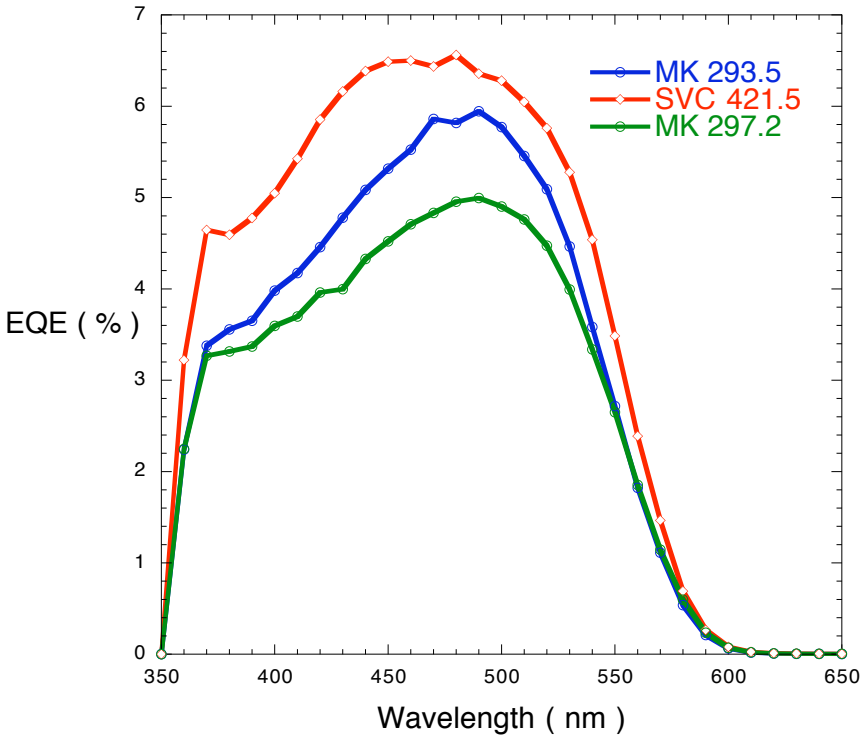

M3EH TiO_x Devices: For this configuration I had a sample set of 5 devices, with peak EQEs ranging form 4.99% at 490nm (MK 297.2) to 6.56% at 480nm (SVC 421.5). The

full EQEs are given for three representative devices in Fig. 12. These results agree well with previous data taken at the National Renewable Energy Lab (NREL) and data from the spectroscopy lab here at UCSC.

Fig.13: M3EH TiO2 EQE Comparison

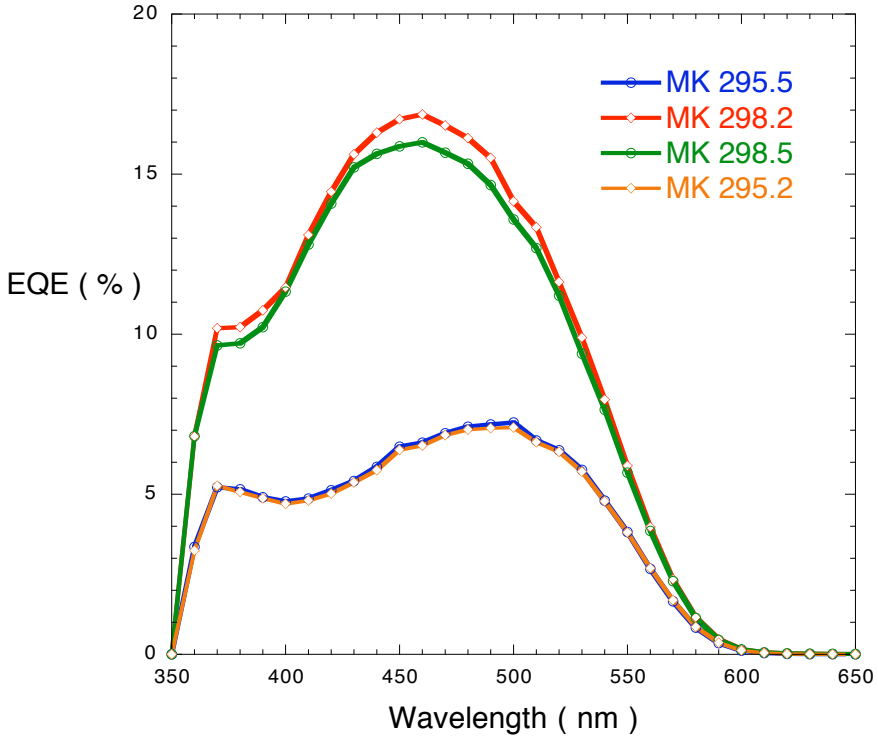

M3EH TiO_2 Devices: For the M3EH nanoparticles devices I had a sample set of only two devices. One of these devices showed a large boost in performance over the M3EH TiO_x devices, with a peak EQE of 16.87% at 460nm (MK 298.2). The second device peaked at only 7.24% at 500nm, however this device still out performed the M3EH TiO_x devices. I attribute the wide range in device performances to the limited size of the sample set. Unfortunately, these devices had to be made on short notice, which prevented me from gathering a larger data set. I believe that additional testing would

have shown that the 16.87% peak EQE of MK 298.2 is more representative of this configuration's performance.

Fig.14: M3EH TiOx / TiO2 EQE Comparison

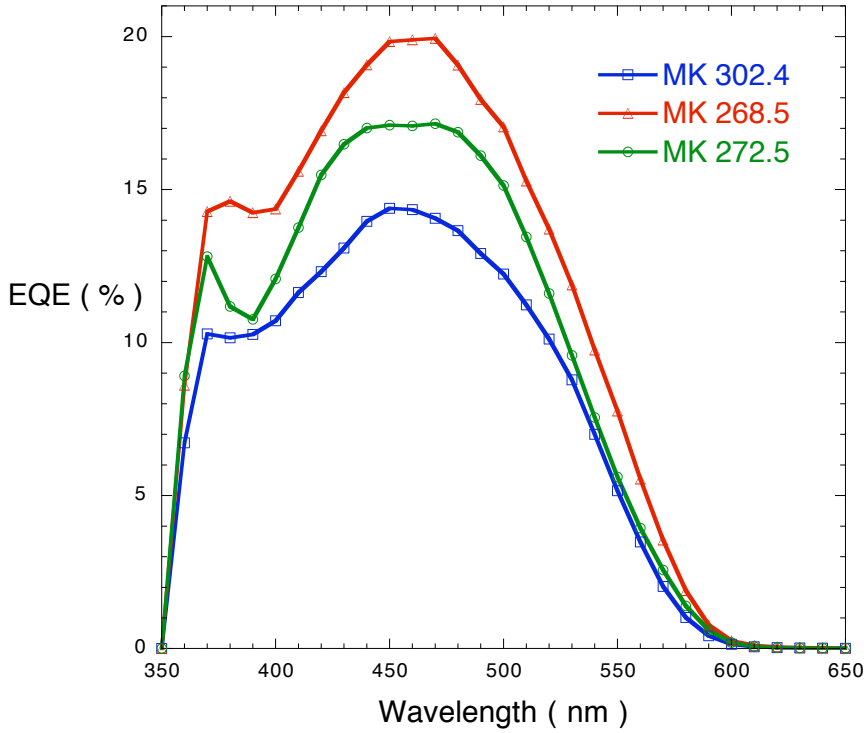

M3EH TiO_X / TiO_2 Devices: For the TiO_x / nanoparticle configuration I had a sample set of five devices. All the devices gave excellent EQE performances, with peak EQEs ranging from 14.39% at 460nm (MK 302.4) to 19.94% at 470nm(MK 268.5). Fig. 14 gives the full EQEs for three representative devices. It is important to note that these five devices where selected from a very large sample. Dr. Kreger has been working for some time on improving the performance of the M3EH TiO_X / TiO_2 configuration and three of the devices I chose to examine were among the best she has manufactured so far.

Fig.15: M3EH Electron-Collector Comparison

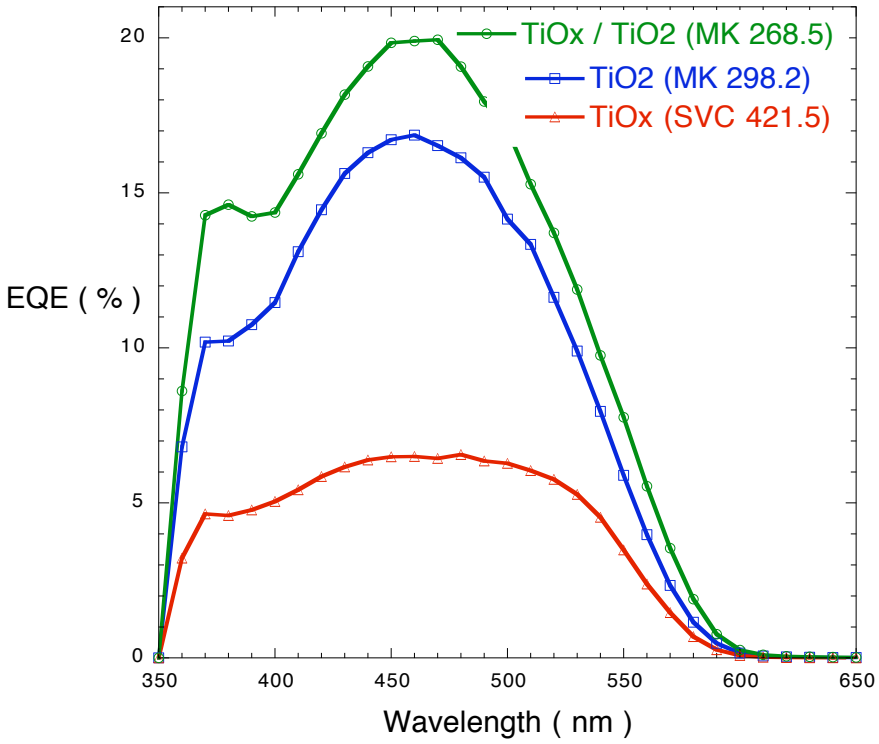

M3EH Electron-Collector Configurations: Fig. 15 illustrated the EQE performances for three M3EH devices, each with a different electron-collector. These devices represent the best EQEs for their respective configurations. This graph demonstrates that a TiO_2 / M3EH interface is significantly more efficient at disassociating excitons than a TiO_x / M3EH interface. It seems that the roughness of the TiO_2 layer, which increases the area of contact with the M3EH, does indeed boost EQE. However, it is the combination TiO_x / TiO_2 collector layer which has the best EQE performance. This suggests that the rough TiO_2 layer needs a more stable and smooth foundation of TiO_x to fully exploit the increased area of the disassociation interface. However, as I noted above, the TiO_x / TiO_2 data came from a much larger sample set than the TiO_2 data. This suggests that the

differences in performance may only be a result of the difference in sample size and that the addition of the TiO_x layer does not actually have a large effect on device performance.

Fig.16: Blend TiOx EQE Comparison

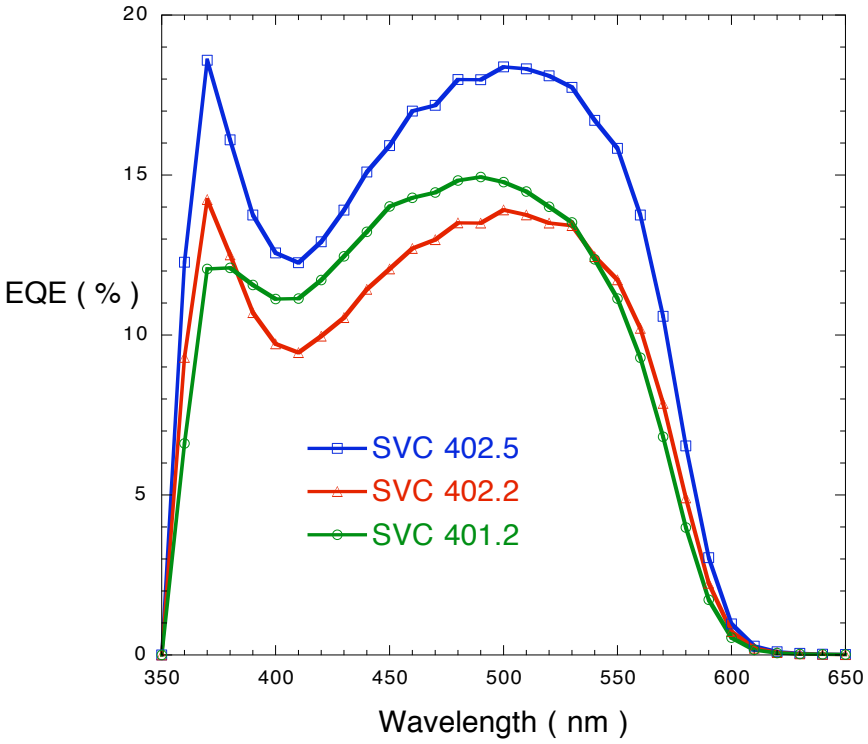

Blend TiO_x Devices: For this device configuration I had a small sample set of two devices. The peak EQE performances ranged from 13.91% at 500nm to 18.38% at 500nm. The Full EQE data is given above in Fig. 16. The graph shows two EQE maxima for each device, unfortunately the solar cell EQE data from NREL cuts off at 400nm, so I have no comparison data for the first maximum. The EQEs for the second maxima are somewhat lower than previous data on SVC blends from NREL, which gave peak EQEs of approximately 25%. However, my devices where manufactured on short notice and time constraints prevented me from testing additional devices of this

configuration. The blend devices are also unstable, with performance usually dropping off after a week or even a day. As a result I was not able to investigate any of the previous high performance SVC devices.

Fig.17: Blend TiO2 EQE Comparison

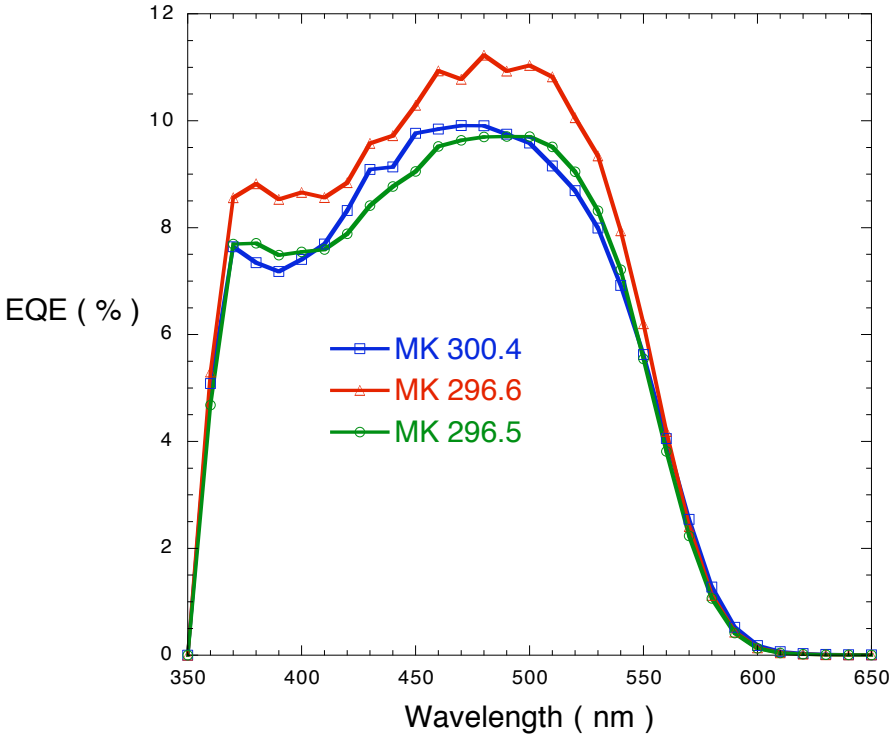

Blend TiO_2 Devices: For the blend nanoparticle devices I had a sample set of 2 devices, with peak EQEs ranging from 9.71% at 490nm (MK 296.5) to 11.23% at 480nm (MK 296.6). Full EQEs are given above in Fig. 17. No previous data was available for comparison and the small size of the sample set makes it difficult to confirm that these performances are typical for the blend nanoparticle configuration. However, it seems that in contrast to M3EH devices, using the rougher TiO_2 layer actually reduces a blended device's performance.

Fig.18: Blend TiOx / TiO2 EQE Comparison

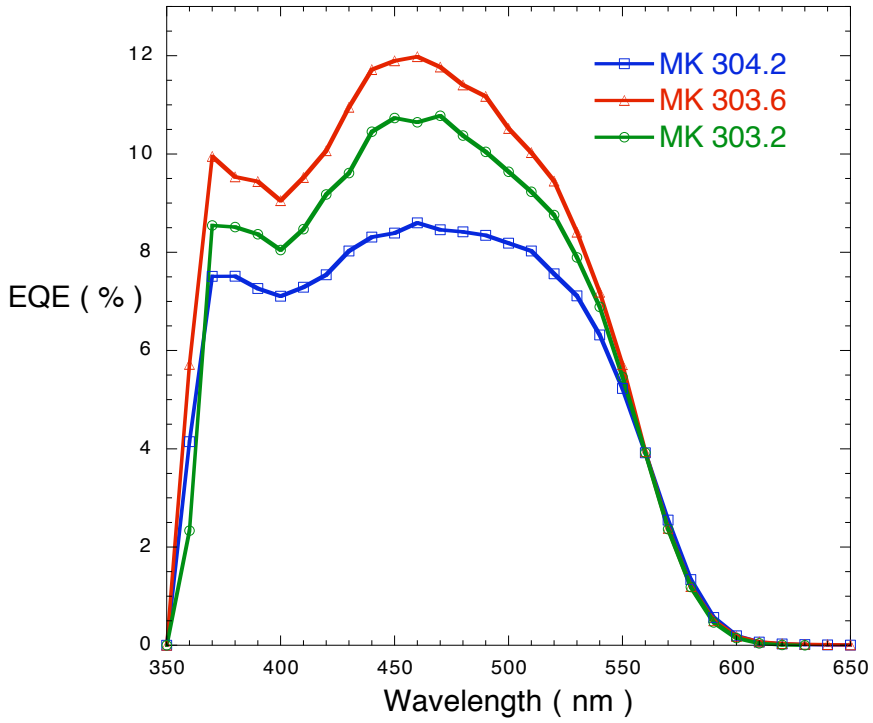

Blend TiO_x / TiO_2 Devices: For the blend TiO_x / nanoparticle configuration I had a sample set of two devices, with peak EQEs ranging from 8.59% at 460nm (MK 304.2) to 11.98% at 460nm (MK 303.6). These EQEs also seem to indicate that the addition of TiO_2 nanoparticle layer actually lowers device performance with respect to the blend TiO_x devices.

Fig.19: Blend Electron-Collector Comparison

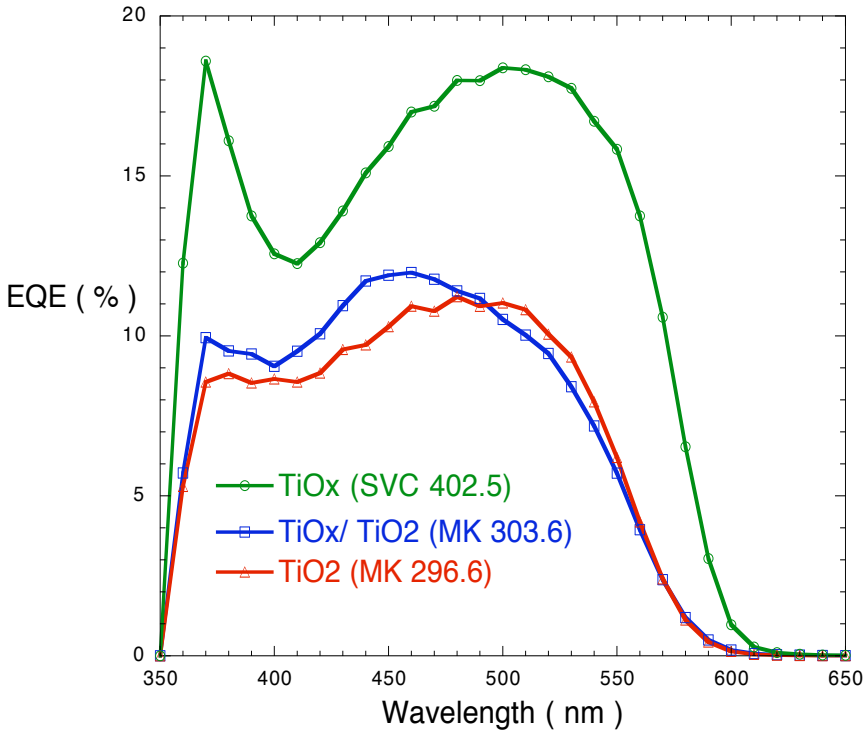

Blend Electron-Collector Configuration: Fig. 19 illustrates the EQE performances for three blend devices, each with a different electron-collector. These devices represent to best EQEs for their respective configurations. In sharp contrast with the M3EH devices, it appears that for blends the TiO_x / polymer interface is significantly more efficient at exciton disassociation than the TiO_2 / polymer interface. As a TiO_2 / M3EH interface has been seen to boost disassociation I assume that the drop in performance is connected to the TiO_2 / Cn –Ether interface in the blended devices. Unfortunately, time constraints prevent any further investigation, but I would have liked to manufacture some straight Cn – Ether devices with both TiO_x and TiO_2 to see what the effect of the different electron-collectors would be on device EQE. My hypothesis is that using a TiO_2 interface with Cn – Ether inhibits exciton disassociation.

Fig.20: M3EH TiOx vs. Blend TiOx

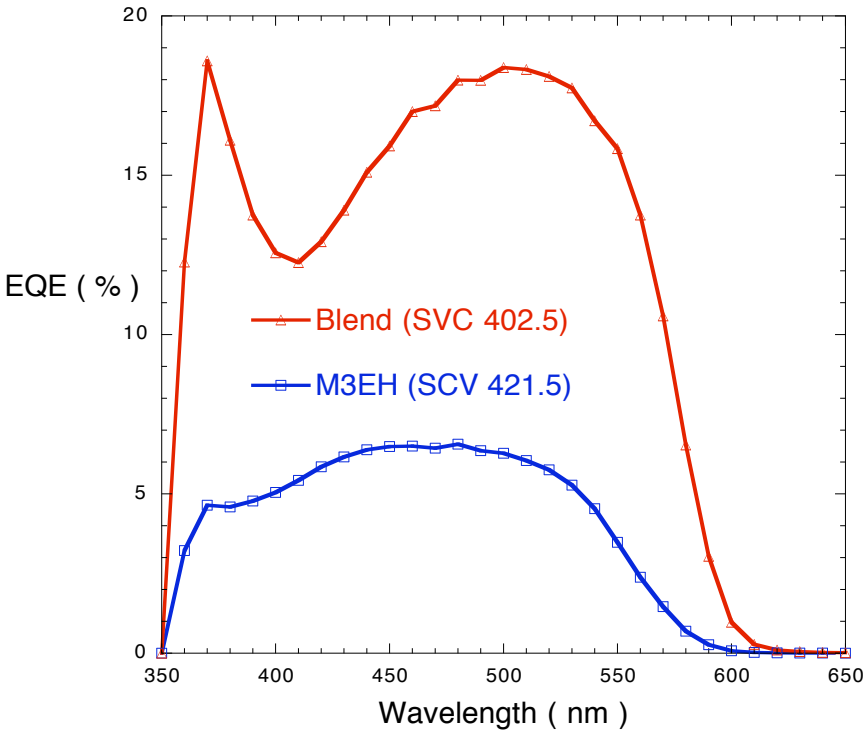

M3EH versus Blend Performances: Fig. 20 gives a direct comparison between M3EH and blend EQEs for the TiO_x electron-collector. Fig. 20 clearly demonstrates that for the TiO_x / polymer configuration, blended M3EH and Cn – Ether outperforms straight M3EH, with a peak EQE of 18.34% for the blend versus 6.56% for M3EH. This seems to support the argument that the blended polymers phase separate and that the large contact area created between theses polymer regions acts as an additional disassociation interface. While the M3EH data for this graph agrees well with previously collected data, the blend data, as noted before is actually lower than data from both NREL and UCSC. This indicates that the performance bonuses of blended M3EH / Cn – Ether are even greater than depicted in Fig. 20.

Fig.21: M3EH TiO2 vs. Blend TiO2

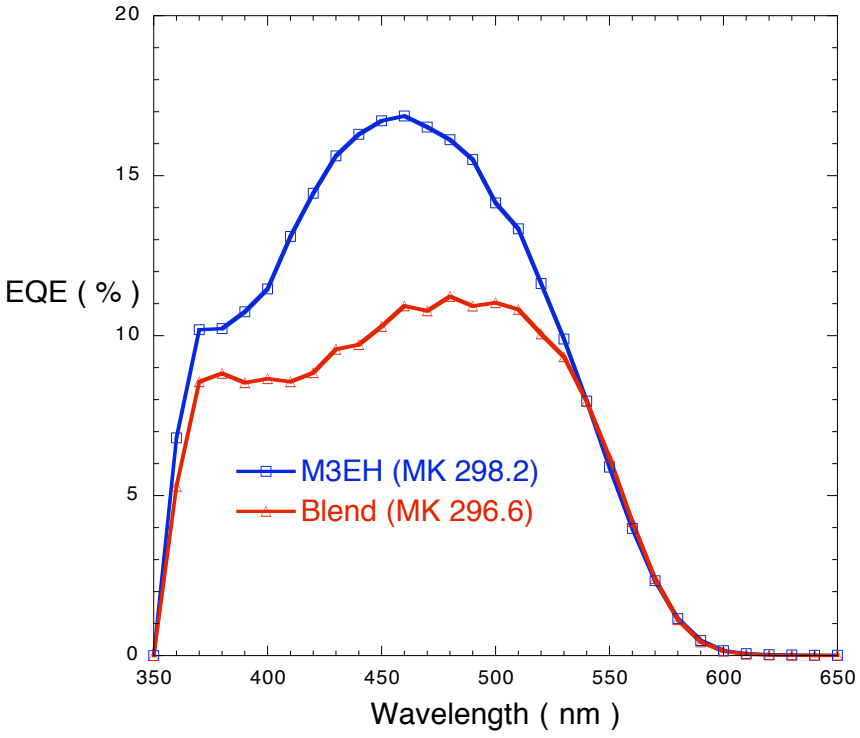

Fig. 22: M3EH TiOx/ TiO2 vs. Blend TiOx/ TiO2

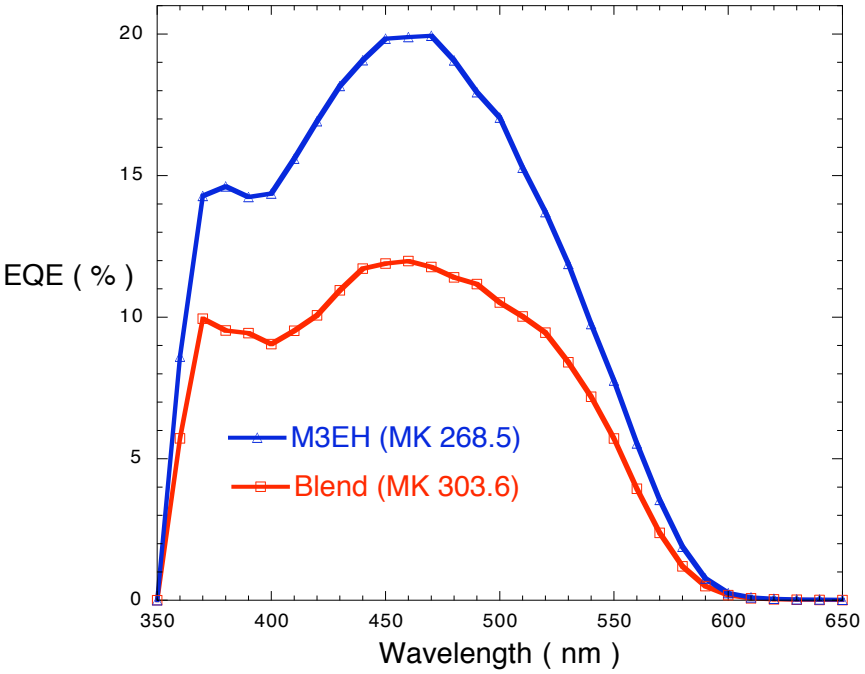

Fig. 21 and Fig. 22 compare blended devices to M3EH devices for the two TiO_2 / polymer interface configurations. These graphs illustrate that for both the TiO_2 and TiO_x / TiO_2 interfaces the straight M3EH devices clearly outperform the blended polymer devices. For the TiO_2 interface M3EH gives a peak EQE of 16.78%, while blended polymer gives only 11.23%. On the TiO_x / TiO_2 interface the difference is even more pronounced with a peak EQE of 19.94% for M3EH versus 11.98% for the blend. Considering that on the TiO_x interface, blended polymer significantly boosted EQE performance, these graph further indicate that the interaction between TiO_2 and Cn – Ether hampers exciton disassociation.

Conclusion:

In conclusion, my investigation of the six polymer solar cell configurations, M3EH TiO_x, M3EH TiO_2, M3EH TiO_x / TiO_2, Blend TiO_x, Blend TiO_2 and Blend TiO_x / TiO_2, has yielded some interesting and hopefully useful results. For polymer solar cells based on straight M3EH – PPV, it has been shown that a TiO_x / TiO_2 / M3EH disassociation interface delivers much higher external quantum efficiencies than a TiO_x / M3EH interface, with EQEs of 19.94% (TiO_x / TiO_2) versus 6.56% (TiO_x). Although the TiO_x / TiO_2 / M3EH configuration delivered the highest EQE for this experiment, I believe that further investigation of the TiO_2 only configuration may yield equally impressive results. The results for the M3EH devices seem to confirm that the roughness of the TiO_2 layer does boost exciton disassociation. For the blended M3EH / Cn – Ether devices the opposite behavior was observed. The Blend TiO_x configuration achieved the best EQE, 16.78%, while Blend TiO_2 gave 11.23% and Blend TiO_x / TiO_2 gave 11.98%.

Considering that blended M3EH / Cn – Ether has been shown to greatly improve EQE on a TiO_x layer (16.78% versus 6.56% for straight M3EH) it seems that the interaction between the Cn – Ether and TiO_2 has a negative affect on exciton disassociation. I would recommend investigating straight Cn – Ether on both TiO_x and TiO_2 layers to see how the EQE is affected. If the TiO_2 EQEs are significantly lower it would explain the drops in blend EQEs that I have observed.

Once again I would like to emphasize that I had to collect most of my data during a very short period, this led to small sample sizes for some of the device configurations, which may have affected to quality of my data. Further investigation into the EQEs of the six device configurations I examined as well as other cell architectures will enhance the understanding of polymer solar cells and help to increase there efficiency. I hope that the photoaction current spectra apparatus, which I assembled for this experiment will aid Dr. Sue Carter in her continuing investigation of polymer solar cells. Maybe the scientific breakthrough, which will allow solar power to take over as the world's key source of energy will take place here at UCSC, then I will have remote bragging rights to making the world a better place.

Thank you:

This report would not be complete with out some very heart-felt thanks. Thank you to Dr. Sue Cater for allowing me to work in your lab, for all your assistance with this project and my grad school applications and for paying me so that I could feed myself you have been a great help and an inspiration to pursue a career in research. Thank you to Dr. Melissa Kreger for teaching me so much, putting up with my endless questions and

for donating your solar cells, I never could have figured out my way around the lab with out your help. Thanks to Stephanie Chasteen, who also donated solar cells, without which my report would have been impossible to complete. Thanks for working late Steph; I hope my data helps you finish your thesis. Thank you to Yuko Nakazawa for helping me with the LabView programming, you saved me weeks of work, good luck finishing up with school. Thank you all the folks in Sue's lab for your help and support, thanks Tosan, Janelle, and Eric. Finally thank you so much to my parents, Robert and Carol and to my beloved brother and sister, Geoffrey and Stephanie. I would have never even tried to come this far with out your love and devotion.

---

[i] Improved Performance Polymer – Inorganic Composite Photovoltaics. Breeze, Allison J. USCS, 2000
[ii] Illustration donated generously by Stephanie V. Chasteen
[iii] TiO_x Layer in Plastic Solar Cells. Omabegha, Tosan UCSC 2002
[iv] TiO_x Layer in Plastic Solar Cells. Omabegha, Tosan UCSC 2002